



Isogeometric analysis of continuum damage in rotation-free composite shells

X. Deng, A. Korobenko, J. Yan, Y. Bazilevs*

Department of Structural Engineering, University of California, San Diego, La Jolla, USA

Available online 28 September 2014

Highlights

- A large-deformation, isogeometric rotation-free shell formulation is equipped with a damage model to simulate progressive failure in composites.
- Four intralaminar modes of failure are considered: Longitudinal and transverse tension, and longitudinal and transverse compression.
- The proposed methodology is valid in the regime of thin shell structures where damage occurs without significant evidence of delamination.
- The damage model is extensively validated against experimental data and its use is also illustrated in the context of multiscale composite damage analysis.

Abstract

A large-deformation, isogeometric rotation-free Kirchhoff–Love shell formulation is equipped with a damage model to efficiently and accurately simulate progressive failure in laminated composite structures. The damage model consists of Hashin’s theory of damage initiation, a bilinear material model for damage evolution, and an appropriately chosen Gibbs free-energy density. Four intralaminar modes of failure are considered: Longitudinal and transverse tension, and longitudinal and transverse compression. The choice of shell formulation and modes of failure modeled make the proposed methodology valid in the regime of relatively thin shell structures where damage occurs without significant evidence of delamination. The damage model is extensively validated against experimental data and its use is also illustrated in the context of multiscale composite damage analysis.

© 2014 Elsevier B.V. All rights reserved.

Keywords: Isogeometric analysis; NURBS; Multiscale modeling; Continuum damage modeling; Laminated composites; Kirchhoff–Love shells

1. Introduction

Damage in composite laminates exhibits complex behavior due to heterogeneous failure mechanisms occurring across different spatial scales. A damage model may be either discrete or continuous depending on the scales involved. The model is typically discrete for atomistic voids and lattice defects, and continuous for micro-, meso-, and

* Corresponding author. Tel.: +1 858 534 3663.

E-mail addresses: yuri@ucsd.edu, jbazilevs@ucsd.edu (Y. Bazilevs).

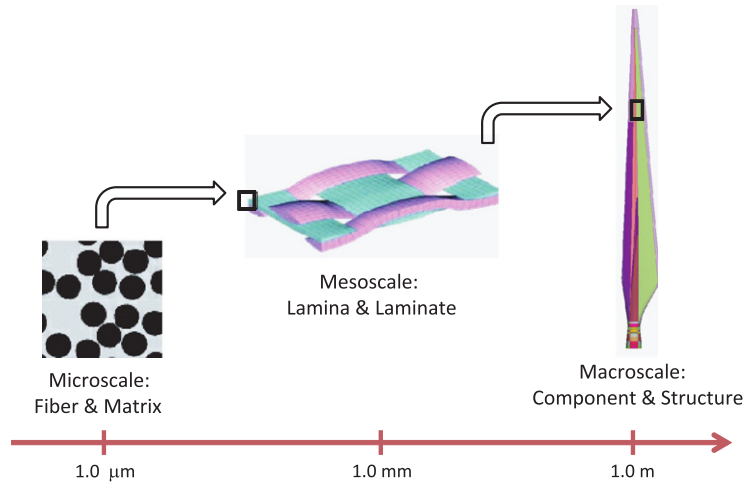


Fig. 1. Illustration of the multiple spatial scales involved in damage modeling of composite shell structures.

macroscales. At the microscale, a representative volume element (RVE) that is both small enough to distinguish the microscopic heterogeneities and large enough to represent the overall behavior of the heterogeneous medium is typically introduced to model phenomena such as separation (or debonding) at the fiber-matrix interface or the initiation, growth, and coalescence of microcracks [1]. At the mesoscale, various modes of damage, such as fiber fracture, matrix cracking, and delamination may be incorporated at the lamina or laminate level. At the macroscale, a composite laminate is typically modeled as a collection of plies, where each ply is an orthotropic medium with continuously distributed material properties and damage indices. (See Fig. 1 for an illustration of the multiscale concept.)

Most research on multiscale composite damage modeling is focused on a two-scale (micro–macro) concept [2,3,1,4]. In [5–7,4] the authors developed a computationally efficient anisotropic homogenization-based continuum model to simulate the fiber-matrix debonding in microstructural damage. The micromechanical model incorporates the path dependence effect by introducing a principal damage coordinate system. To overcome the limitation of the RVE periodicity, a hierarchical model consisting of multiple adaptive levels was conducted by the Voronoi-cell finite element method. In [3,1] the authors developed a homogenization method based on a two-scale asymptotic expansion of the damage tensor in a heterogeneous medium, which led to closed-form expressions relating local (microscopic) fields to overall (macroscopic) strains and damage. However, for certain composite systems, such as woven composites, the two-scale model is insufficient to describe the presence of strong heterogeneities. Refs. [3,1] further extended the two-scale damage theory to the three-scale theory by adding a larger-scale RVE on a mesoscopic scale. Similarly, the triple-scale asymptotic expansion of damage tensor has led to a closed form expression relating the local (microscopic and mesoscopic) fields to the global (macroscopic) strains and damage.

Localization of deformation may occur during failure when high straining is developed in a small region of the material, while the rest of the structure experiences normal strain levels. A sharp decrease of loading capacity due to localization of deformation is termed strain softening [8,9]. Strain softening may lead to an ill-posed boundary value problem because the governing partial differential equations lose ellipticity for the static case and hyperbolicity for the dynamic case. Furthermore, high mesh sensitivity is sometimes observed in numerical simulations in the presence of strain localization. One successful remedy for this is a regularization technique that arises from nonlocal damage theory first introduced in [8,9]. Subsequently, in [10,11] the authors successfully used gradient-enhanced damage and plasticity models to control localization of deformation. In [12] the authors used Isogeometric Analysis (IGA) [13,14] based on Non-Uniform Rational B-Splines (NURBS) [15] to formulate and study higher-order gradient damage approximations that require higher-order smoothness of the underlying spatial discretization. In recent work [16], the authors incorporated gradient damage models into continuum shell elements.

In this paper, motivated by the multiscale modeling paradigm, we focus on the meso- and macroscale continuum damage mechanics (CDM) of composite lamina and laminates. Our main interests lie in the modeling of aerospace and civil engineering structures, which are often thin and curved laminated composite shells (see, e.g., [17] and Fig. 1). The recent successful application of IGA to thin shells in [18–23], including composite laminates in [24,25], and the recent work on CDM in composites [26] enable a formulation of an accurate and efficient damage modeling

framework. The CDM model presented in this work is comprised of the following constituents: Hashin's theory [27] is chosen to model damage initiation, Gibbs free energy and the corresponding damage elasticity matrix are taken from [28], and a well-known bilinear material law is chosen to model damage evolution. A similar damage model that uses these constituents is presented [26]. As a result, this work is not focused on the development of a novel damage model, but rather in adapting the damage model to large-deformation rotation-free IGA composite shells, and performing its careful validation.

Delamination is known to be a very important failure mechanism for laminated composites. It involves the initiation and propagation of cracks running in the interlaminar region. It is more likely to occur with short spans, in thick laminates, or in composite with lower interlaminar shear strength [29]. Delamination is not considered in the present paper and thus the range of validity of the proposed formulation involves relatively thin laminates with high interlaminar shear strength.

The paper is organized as follows. In Section 2, the formulation of a rotation-free Kirchhoff–Love shell from [18,19] is recalled in some detail. In Section 3, a progressive damage model based on the property-degradation CDM at the meso- and macroscale is presented. A step-by-step implementation of the damage model is also provided. In Section 4, the model and its discretization using NURBS-based IGA is validated using experimental results from two carbon-fiber-reinforced laminates that were tested to failure. An example involving a composite plate subject to out-of-plane loading is also presented in this section to illustrate the use of a multiscale modeling paradigm in IGA-based progressive damage simulation in composites. In Section 5, discussion of the results is provided, conclusions are drawn, and future research directions are presented.

2. Isogeometric Kirchhoff–Love shell

In this section we use IGA to model shell structures that are governed by the Kirchhoff–Love shell theory [18,19]. The Kirchhoff–Love shell theory assumes that the fibers that are initially straight and normal to the shell midsurface remain straight and normal to the shell midsurface throughout the deformation. This implies that transverse shear strains are neglected, making the theory applicable to thin shells [30]. Many shell structures of practical engineering interest satisfy this criterion. Thin shells have an optimal load-carrying behavior and therefore allow the construction of highly efficient light-weight structures [31,32]. In the governing equations of the Kirchhoff–Love shell expressed in terms of the midsurface displacements, second order derivatives with respect to the parametric coordinates of the midsurface appear, and therefore C^1 -continuity of the approximation functions is required for the discrete formulation to be conforming. NURBS basis functions have the necessary smoothness at the patch level. NURBS are inherently higher order, which also alleviates locking associated with low-order shell discretizations. The attractive feature of the Kirchhoff–Love theory is that the formulation is purely displacement-based and no rotational degrees of freedom are necessary [33–35].

The variational formulation for a Kirchhoff–Love shell is based on the principle of virtual work and is expressed as

$$\delta W = \delta W_{int} + \delta W_{ext} = 0, \quad (1)$$

where W , W_{int} , and W_{ext} denote the total, internal, and external work, respectively, and δ denotes a variation with respect to the virtual displacement variables $\delta \mathbf{y}$, that is

$$\delta W = \frac{\partial W}{\partial \mathbf{y}} \delta \mathbf{y}. \quad (2)$$

The internal virtual work is given by

$$\delta W_{int} = - \int_{\Omega_0} (\mathbf{S} : \delta \mathbf{E}) \, d\Omega, \quad (3)$$

where Ω_0 is the shell volume in the reference configuration (the total Lagrangian approach is adopted in this work [36]), \mathbf{E} is the Green–Lagrange strain tensor, $\delta \mathbf{E}$ is its variation, and \mathbf{S} is the second Piola–Kirchhoff stress tensor.

For shell theory, the three-dimensional continuum description is reduced to that of the shell midsurface. Only in-plane stress and strain tensors are considered, and Greek indices, $\alpha = 1, 2$ and $\beta = 1, 2$, are employed to denote their components.

The components of the Green–Lagrange strain tensor are separated into two parts corresponding to membrane and bending action as follows:

$$E_{\alpha\beta} = \varepsilon_{\alpha\beta} + \xi_3 \kappa_{\alpha\beta}, \tag{4}$$

where $\xi_3 \in [-0.5h_{th}, 0.5h_{th}]$ is the through-thickness coordinate, h_{th} is the local shell thickness, $\varepsilon_{\alpha\beta}$ are the membrane strains given by

$$\varepsilon_{\alpha\beta} = \frac{1}{2}(g_{\alpha\beta} - G_{\alpha\beta}), \tag{5}$$

and $\kappa_{\alpha\beta}$ are the changes in curvature defined as

$$\kappa_{\alpha\beta} = b_{\alpha\beta} - B_{\alpha\beta}. \tag{6}$$

In (5), the covariant metric tensors are given by

$$g_{\alpha\beta} = \mathbf{g}_\alpha \cdot \mathbf{g}_\beta = \mathbf{x}_{,\alpha} \cdot \mathbf{x}_{,\beta}, \tag{7}$$

$$G_{\alpha\beta} = \mathbf{G}_\alpha \cdot \mathbf{G}_\beta = \mathbf{X}_{,\alpha} \cdot \mathbf{X}_{,\beta}, \tag{8}$$

and in (6), the curvature tensors are defined as

$$b_{\alpha\beta} = -\mathbf{g}_{\alpha,\beta} \cdot \mathbf{g}_3, \tag{9}$$

$$B_{\alpha\beta} = -\mathbf{G}_{\alpha,\beta} \cdot \mathbf{G}_3, \tag{10}$$

where \mathbf{x} and \mathbf{X} are the position vectors of material points in the current and reference configuration, respectively, and $(\cdot)_{,\alpha}$ denotes partial differentiation with respect to the midsurface parametric coordinates. In Eqs. (9)–(10), \mathbf{g}_3 and \mathbf{G}_3 are the unit vectors in the direction normal to the shell midsurface in the current and reference configurations, respectively.

In Eq. (4), the components of the Green–Lagrange strain tensor are given with respect to the contravariant basis vectors \mathbf{G}^α that are related to the covariant basis vectors \mathbf{G}_β as

$$\mathbf{G}^\alpha = [G_{\alpha\beta}]^{-1} \mathbf{G}_\beta. \tag{11}$$

Given the covariant basis, we define the local orthonormal basis $\bar{\mathbf{e}}_\alpha$ by orienting it on \mathbf{G}_1 as follows:

$$\bar{\mathbf{e}}_1 = \frac{\mathbf{G}_1}{\|\mathbf{G}_1\|}, \tag{12}$$

$$\bar{\mathbf{e}}_2 = \frac{\mathbf{G}_2 - (\mathbf{G}_2 \cdot \bar{\mathbf{e}}_1)\bar{\mathbf{e}}_1}{\|\mathbf{G}_2 - (\mathbf{G}_2 \cdot \bar{\mathbf{e}}_1)\bar{\mathbf{e}}_1\|}. \tag{13}$$

We assume the St. Venant–Kirchhoff material law, which we express using the local coordinate system (i.e., coordinate system given by Eqs. (12)–(13)) as

$$\bar{\mathbf{S}} = \bar{\mathbf{C}} \bar{\mathbf{E}}, \tag{14}$$

where $\bar{\mathbf{C}}$ is the constitutive matrix.

Introducing Eqs. (4) and (14) into the expression for the internal virtual work given by Eq. (3), and pre-integrating through the shell thickness, we obtain

$$\begin{aligned} \delta W_{int} &= - \int_{\Omega_0} (\mathbf{S} : \delta \mathbf{E}) \, d\Omega \\ &= - \int_{\Gamma_0^s} \left(\int_{h_{th}} \delta \bar{\mathbf{E}} \cdot \bar{\mathbf{C}} \bar{\mathbf{E}} \, d\xi_3 \right) \, d\Gamma \\ &= - \int_{\Gamma_0^s} \delta \bar{\boldsymbol{\varepsilon}} \cdot \left(\left(\int_{h_{th}} \bar{\mathbf{C}} \, d\xi_3 \right) \bar{\boldsymbol{\varepsilon}} + \left(\int_{h_{th}} \xi_3 \bar{\mathbf{C}} \, d\xi_3 \right) \bar{\boldsymbol{\kappa}} \right) \, d\Gamma \\ &\quad - \int_{\Gamma_0^s} \delta \bar{\boldsymbol{\kappa}} \cdot \left(\left(\int_{h_{th}} \xi_3 \bar{\mathbf{C}} \, d\xi_3 \right) \bar{\boldsymbol{\varepsilon}} + \left(\int_{h_{th}} \xi_3^2 \bar{\mathbf{C}} \, d\xi_3 \right) \bar{\boldsymbol{\kappa}} \right) \, d\Gamma, \end{aligned} \tag{15}$$

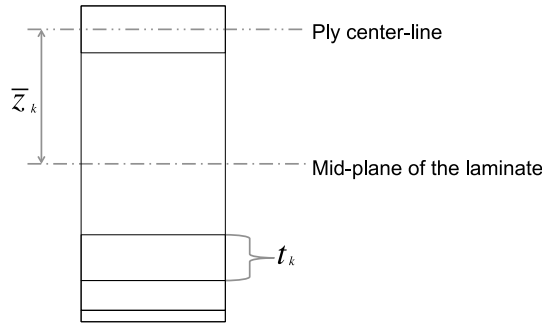


Fig. 2. Composite layup with nonuniform and nonsymmetric distribution of the lamina.

where $\bar{\boldsymbol{\epsilon}}$ and $\bar{\boldsymbol{\kappa}}$ are the vectors of membrane strain and curvature tensor coefficients in the local coordinate system, and $d\Gamma$ is the differential area of the shell midsurface. We denote by Γ_0^s and Γ_t^s the structure midsurface in the reference and deformed configuration, respectively. Furthermore, Γ_0^b denotes the bending strip domain, which is the union of the bending-strip-patch subdomains [19]. The rotation-free Kirchhoff–Love shell formulation at the space-discrete level may now stated as follows: find the displacement of the shell midsurface \mathbf{y}^h , such that $\forall \mathbf{w}^h$,

$$\int_{\Gamma_t^s} \mathbf{w}^h \cdot \rho h_{th} \left(\frac{d^2 \mathbf{y}^h}{dt^2} - \mathbf{f}^h \right) d\Gamma + \int_{\Gamma_0^s} \delta \bar{\boldsymbol{\epsilon}}^h \cdot \left(\mathbf{A} \bar{\boldsymbol{\epsilon}}^h + \mathbf{B} \bar{\boldsymbol{\kappa}}^h \right) d\Gamma + \int_{\Gamma_0^b} \delta \bar{\boldsymbol{\kappa}}^h \cdot \left(\mathbf{B} \bar{\boldsymbol{\epsilon}}^h + \mathbf{D} \bar{\boldsymbol{\kappa}}^h \right) d\Gamma + \int_{\Gamma_0^b} \delta \bar{\boldsymbol{\kappa}}^h \cdot \mathbf{D}^b \bar{\boldsymbol{\kappa}}^h d\Gamma - \int_{(\Gamma_t^s)_h} \mathbf{w}^h \cdot \mathbf{h}^h d\Gamma = 0. \tag{16}$$

In the above formulation, ρ is the through-thickness-averaged density, and $\delta \bar{\boldsymbol{\epsilon}}^h$ and $\delta \bar{\boldsymbol{\kappa}}^h$ are the variations of the membrane-strain and curvatures-change vectors, respectively. $(\Gamma_t^s)_h$ is the shell subdomain with a prescribed traction boundary condition, and \mathbf{h}^h is the prescribed traction vector.

To model a composite shell, classical laminated plate theory [37] is employed. We denote the thickness of the k th ply by t_k , and its centroid by \bar{z}_k (see Fig. 2). With these definitions, in Eq. (16), the extensional, coupling, and bending stiffnesses, given by \mathbf{A} , \mathbf{B} , and \mathbf{D} matrices, respectively, may be computed for any layup as

$$\mathbf{A} = \int_{h_{th}} \bar{\mathbf{C}} d\xi_3 = \sum_{k=1}^n \bar{\mathbf{C}}_k t_k, \tag{17}$$

$$\mathbf{B} = \int_{h_{th}} \xi_3 \bar{\mathbf{C}} d\xi_3 = \sum_{k=1}^n \bar{\mathbf{C}}_k t_k \bar{z}_k, \tag{18}$$

$$\mathbf{D} = \int_{h_{th}} \xi_3^2 \bar{\mathbf{C}} d\xi_3 = \sum_{k=1}^n \bar{\mathbf{C}}_k \left(t_k \bar{z}_k^2 + \frac{t_k^3}{12} \right). \tag{19}$$

Here, $\bar{\mathbf{C}}_k$ is a constitutive material matrix for the k th ply in the local coordinate system given by

$$\bar{\mathbf{C}}_k = \mathbf{T}^T(\phi_k) \tilde{\mathbf{C}}_k \mathbf{T}(\phi_k), \tag{20}$$

$$\mathbf{T}(\phi) = \begin{bmatrix} \cos^2 \phi & \sin^2 \phi & \sin \phi \cos \phi \\ \sin^2 \phi & \cos^2 \phi & -\sin \phi \cos \phi \\ -2 \sin \phi \cos \phi & 2 \sin \phi \cos \phi & \cos^2 \phi - \sin^2 \phi \end{bmatrix}, \tag{21}$$

where ϕ denotes the fiber orientation angle in the ply, and $\tilde{\mathbf{C}}$ is the constitutive matrix for the orthotropic material written with respect to the principal material axes (or lamina axes) of the ply (see [19] for more details). For a general

orthotropic material, in the case of no damage,

$$\tilde{\mathbf{C}} = \begin{bmatrix} \frac{E_1}{(1 - \nu_{12}\nu_{21})} & \frac{\nu_{21}E_1}{(1 - \nu_{12}\nu_{21})} & 0 \\ \frac{\nu_{12}E_2}{(1 - \nu_{12}\nu_{21})} & \frac{E_2}{(1 - \nu_{12}\nu_{21})} & 0 \\ 0 & 0 & G_{12} \end{bmatrix}, \quad (22)$$

where E_1 and E_2 are the Young moduli in the fiber and matrix directions, respectively, ν 's are the Poisson ratios, G_{12} is the shear modulus, and $\nu_{21}E_1 = \nu_{12}E_2$ to ensure the symmetry of the constitutive matrix. The case with damage is discussed in the next section.

3. Continuum damage model

This section presents progressive damage modeling in composite lamina/laminate through property-degradation CDM.

3.1. Damage mechanisms in laminated composite structures

High-fidelity simulation of composites provides better understanding of the structural and material behavior required for advancement of product design. The complexity of strength prediction, even under in-plane loading, lies in various modes of damage, such as fiber fracture, matrix cracking and delamination, which cooperatively lead to loss of loading capacity and structural integrity. In this paper, we focus on *intralaminar* failure mechanisms in laminated composites where there is little evidence of delamination. We also assume that the intralaminar damage modes, namely fiber fracture and matrix cracking, may be isolated. Therefore, damage of each lamina in a composite laminate can be treated individually.

Typical composite lamina and laminate failure modes are presented in Fig. 3. Tensile failure in the longitudinal (i.e., fiber) direction is typically due to stress concentration, and often leads to a “domino effect” where failure of one fiber sets off damage in the adjacent fibers, as shown in Fig. 3(e). Different mechanisms of longitudinal compressive failure include fiber crushing for Kevlar, plastic microbuckling for carbon-fiber-reinforced polymers (CFRPs), and longitudinal cracking for ceramic matrix composites. Plastic microbuckling, the most common compressive failure mode in engineering materials, leads to the formation of kink bands, i.e., buckling of individual fibers in a microbuckle band accompanied by matrix plastic deformation (see Fig. 3(c)). In the presence of in-plane shear stresses, small defects within a ply, such as fiber-resin debonds and resin-starved regions, may trigger a transverse crack that extends through the thickness of the ply without disturbing the fibers. The cracks may first occur at the fiber-matrix interface and in the matrix, and the nucleation and growth of microcracks leads to final failure. Especially in the case of transverse compression, failure is caused by high interfacial shear at a 45° angle to the loading direction (see Fig. 3(d)).

3.2. Damage initiation

Failure of a composite (i.e., the complete loss of its loading capacity) results from progressive degradation of the material stiffness. The onset of degradation or damage initiation is determined in the stress space. Many criteria to predict failure onset in laminated composites, are presented and validated in several references (see, e.g., [41,42]). In the present work we use Hashin's theory of damage initiation [27], which takes into account four intralaminar modes of failure: longitudinal tension (or so-called fiber tension ‘ft’), longitudinal compression (or so-called fiber compression ‘fc’), transverse tension (or so-called matrix tension ‘mt’) and transverse compression (or so-called matrix compression ‘mc’). There are four damage initiation functions F_i ($i = 1+, 1-, 2+, 2-$) associated with the four damage mechanisms, which are defined as follows:

- Longitudinal tension ($\hat{S}_{11} \geq 0$):

$$F_{1+} = \left(\frac{\hat{S}_{11}}{X_T} \right)^2. \quad (23)$$

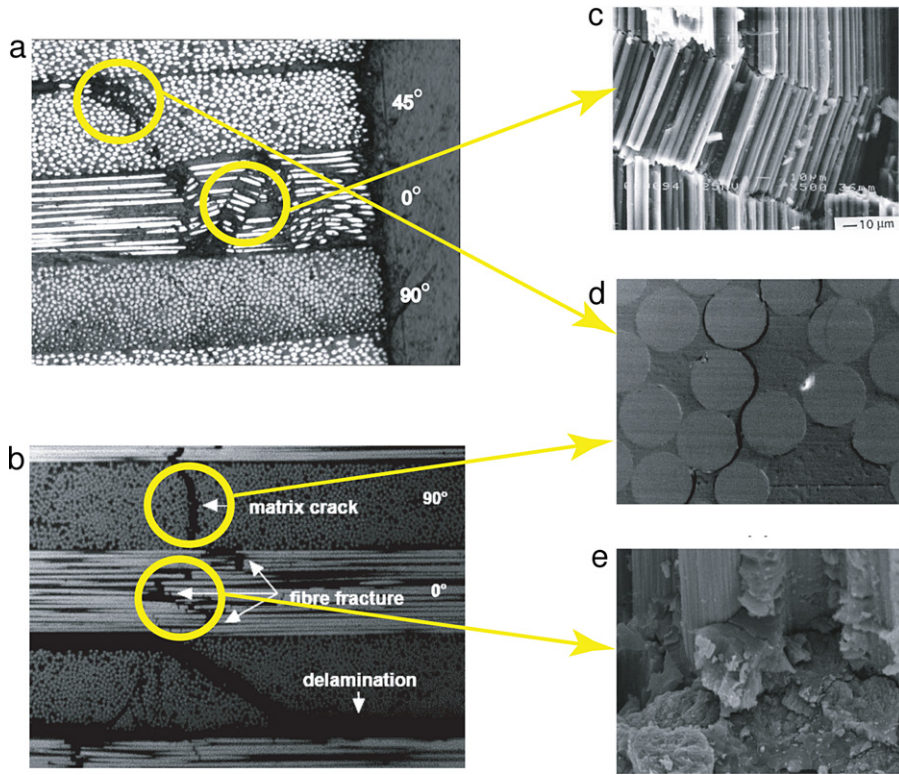


Fig. 3. Failure modes in composite lamina and laminates: (a) Failure mode of composite laminate 1 (from [38]); (b) Failure mode of composite laminate 2 (from [38]); (c) Kink band (from [39]); (d) Matrix crack (from [38]); (e) Fiber fracture (from [40]).

- Longitudinal compression ($\hat{S}_{11} < 0$):

$$F_{1-} = \left(\frac{\hat{S}_{11}}{X_C} \right)^2. \tag{24}$$

- Transverse tension ($\hat{S}_{22} \geq 0$):

$$F_{2+} = \left(\frac{\hat{S}_{22}}{Y_T} \right)^2 + \left(\frac{\hat{S}_{12}}{Z_L} \right)^2. \tag{25}$$

- Transverse compression ($\hat{S}_{22} < 0$):

$$F_{2-} = \left(\frac{\hat{S}_{22}}{Y_C} \right)^2 + \left(\frac{\hat{S}_{12}}{Z_L} \right)^2. \tag{26}$$

Here X_T and X_C denote the longitudinal tensile and compressive strength, respectively, Y_T and Y_C denote the transverse tensile and compressive strength, respectively, and Z_L denotes the longitudinal shear strength. This damage initiation model, which we use in this paper, was first proposed in [27].

The damage initiation functions F_i are expressed in terms of the so-called *effective* second Piola–Kirchhoff stress, which is related to its *nominal* counterpart as

$$\begin{bmatrix} \hat{S}_{11} \\ \hat{S}_{22} \\ \hat{S}_{12} \end{bmatrix} = \mathbf{M} \begin{bmatrix} \tilde{S}_{11} \\ \tilde{S}_{22} \\ \tilde{S}_{12} \end{bmatrix}. \tag{27}$$

Here \tilde{S} 's are the components of the nominal second Piola–Kirchhoff stress with respect to the principal material axes,

$$\mathbf{M} = \begin{bmatrix} \frac{1}{1-d_1} & 0 & 0 \\ 0 & \frac{1}{1-d_2} & 0 \\ 0 & 0 & \frac{1}{1-d_6} \end{bmatrix} \tag{28}$$

is the *damage operator*, and d_1 , d_2 , and d_6 are the damage indices, which we define in the next section. The concept of nominal stress is standard in CDM and reflects the reduction of load-carrying net area due to the formation of distributed microcracks and voids during damage (see [43] and references therein for detailed discussion). It is the nominal stress that drives the damage initiation and evolution.

3.3. Gibbs free energy and the damage elasticity matrix

The Gibbs free-energy density (per unit volume) of the undeformed configuration for a damaged orthotropic material may be defined as

$$G = \frac{1}{2E_1} \left(\frac{\tilde{S}_{11}^2}{1-d_1} \right) + \frac{1}{2E_2} \left(\frac{\tilde{S}_{22}^2}{1-d_2} \right) - \frac{\nu_{12}}{E_1} \tilde{S}_{11} \tilde{S}_{22} + \frac{\tilde{S}_{12}^2}{2(1-d_6)G_{12}}, \tag{29}$$

where d_i ($i = 1, 2, 6$) are the damage indices associated with the fiber and matrix directions, and in-plane shear, respectively. The expression given by Eq. (29) was proposed in [28]. In order to have a thermodynamically-consistent formulation the following inequality must hold:

$$\dot{G} = \frac{\partial G}{\partial d_1} \dot{d}_1 + \frac{\partial G}{\partial d_2} \dot{d}_2 + \frac{\partial G}{\partial d_6} \dot{d}_6 \geq 0, \tag{30}$$

where the “dot” denotes a generic rate of change (such as, for example, the time rate of change). As a result, the choice of the Gibbs free-energy density given by Eq. (29) and the above inequality imply that $\dot{d}_1 \geq 0$, $\dot{d}_2 \geq 0$, and $\dot{d}_6 \geq 0$. That is, the damage evolution law should be chosen in such a way that the damage indices do not decrease. (We discuss the damage evolution law in the next section.)

The Green–Lagrange strain may be expressed as the first partial derivative of the Gibbs free energy density with respect to the second Piola–Kirchhoff stress as

$$\tilde{\mathbf{E}} = \frac{\partial G}{\partial \tilde{\mathbf{S}}}, \tag{31}$$

and the corresponding compliance matrix in lamina coordinates $\tilde{\mathbf{H}}$ may be expressed as the second partial derivative of the Gibbs free energy density with respect to the second Piola–Kirchhoff stress as

$$\tilde{\mathbf{H}} = \frac{\partial^2 G}{\partial \tilde{\mathbf{S}} \partial \tilde{\mathbf{S}}}. \tag{32}$$

Direct computation of the compliance matrix gives

$$\tilde{\mathbf{H}} = \begin{bmatrix} \frac{1}{(1-d_1)E_1} & -\frac{\nu_{21}}{E_2} & 0 \\ -\frac{\nu_{12}}{E_1} & \frac{1}{(1-d_2)E_2} & 0 \\ 0 & 0 & \frac{1}{(1-d_6)G_{12}} \end{bmatrix}. \tag{33}$$

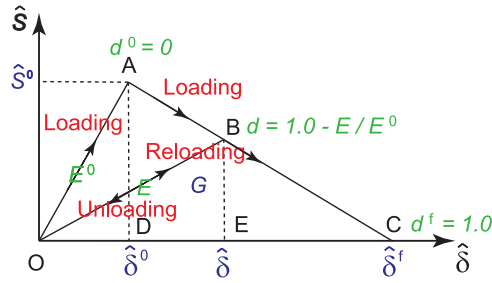


Fig. 4. Illustration of a bilinear material model that governs damage evolution.

The damage elasticity constitutive tensor in lamina coordinates $\tilde{\mathbf{C}}$ may now be computed as the inverse of the compliance matrix, and is given by

$$\tilde{\mathbf{C}} = \frac{1}{D} \begin{bmatrix} (1 - d_1)E_1 & (1 - d_1)(1 - d_2)v_{21}E_1 & 0 \\ (1 - d_1)(1 - d_2)v_{12}E_2 & (1 - d_2)E_2 & 0 \\ 0 & 0 & D(1 - d_6)G_{12} \end{bmatrix}, \tag{34}$$

where $D = 1 - (1 - d_1)(1 - d_2)v_{12}v_{21}$. Finally, damage indices d_1-d_6 are computed from damage variables $d_{1+}, d_{1-}, d_{2+}, d_{2-}$, corresponding to the four failure modes as follows:

$$d_1 = \begin{cases} d_{1+} & \hat{S}_{11} \geq 0 \\ d_{1-} & \hat{S}_{11} < 0, \end{cases} \tag{35}$$

$$d_2 = \begin{cases} d_{2+} & \hat{S}_{22} \geq 0 \\ d_{2-} & \hat{S}_{22} < 0, \end{cases} \tag{36}$$

and

$$d_6 = 1 - (1 - d_{1+})(1 - d_{1-})(1 - d_{2+})(1 - d_{2-}). \tag{37}$$

The evolution of the above introduced damage variables is described in the following section.

3.4. Damage evolution

The damage evolution model is based on the traction–separation relationship employed in cohesive-zone modeling [26]. In this work a bilinear model is assumed (i.e., linear-elastic behavior followed by linear softening), and is illustrated in Fig. 4. In this simple 1D setting the damage variable d is defined as $1 - E/E^0$, where E^0 is the initial stiffness, and E is the current stiffness after damage occurred. Note that, in 1D, for a single failure mode, the damage variable and damage index are coincident. Rearranging terms yields $E = (1 - d)E^0$, which gives the interpretation of d as the degree to which the initial stiffness is degraded. In the bilinear model, during loading, the initial modulus E^0 remains constant until the equivalent displacement $\hat{\delta}$ reaches $\hat{\delta}^0$, and the equivalent stress \hat{S} reaches the material strength \hat{S}^0 , a location given by point A in Fig. 4. When loading continues beyond point A and reaches point B in the figure, stiffness E is reduced according to the linear softening law. Other softening laws are also possible (see, e.g., [44]). The material is completely damaged at point C in the figure, where the equivalent displacement reaches its final value (i.e., $\hat{\delta} = \hat{\delta}^f$), and $d = 1$. It is often useful to define the damage displacement ratio as the ratio of the final equivalent displacement to its initial counterpart, $r = \hat{\delta}^f/\hat{\delta}^0$. This ratio is always greater than unity, and values close to unity produce a more abrupt transition to a fully damaged state.

In Fig. 4, the initial stiffness E^0 is given by $\frac{AD}{OD}$, and the current stiffness E is given by $\frac{BE}{OE}$, which gives

$$\frac{E}{E^0} = \frac{\overline{BE}}{\overline{AD}} \cdot \frac{\hat{\delta}^0}{\hat{\delta}}. \tag{38}$$

Using the similarity of triangles ADC and BEC, we obtain

$$\frac{\overline{BE}}{\overline{AD}} = \frac{\hat{\delta}^f - \hat{\delta}}{\hat{\delta}^f - \hat{\delta}^0}. \quad (39)$$

Combining the above two equations leads to

$$d = 1 - \frac{E}{E^0} = \frac{\hat{\delta}^f (\hat{\delta} - \hat{\delta}^0)}{\hat{\delta} (\hat{\delta}^f - \hat{\delta}^0)}, \quad (40)$$

which gives the damage variable as a function of the equivalent displacement only. For a thermodynamically consistent formulation, the damage variable can only increase. Therefore, considering a no-recovery damage model, the damage variable may be defined as

$$d = \max \left(d_{\text{old}}, \frac{\hat{\delta}^f (\hat{\delta} - \hat{\delta}^0)}{\hat{\delta} (\hat{\delta}^f - \hat{\delta}^0)} \right), \quad (41)$$

where d_{old} is its previously attained value. The physical meaning of Eq. (41) is that the material in question unloads to the origin, and reloading takes place along the path of maximum damage that occurred previously. The initial equivalent displacement $\hat{\delta}^0$ depends on the initial stiffness E^0 and the material strength \hat{S}^0 . The area of the triangle OAC in the figure corresponds to the fracture energy $G = \int_0^{\hat{\delta}^f} \hat{S}(\hat{\delta}) d\hat{\delta}$. As a result, the final equivalent displacement may be computed as $\hat{\delta}^f = \frac{2G}{\hat{S}^0}$.

In order to fully define the damage model, the initial stiffness, strength, and fracture energy need to be specified for each damage mode. The damage evolution law given by Eq. (41) is applied to each damage mode considered. Furthermore, rather than working with equivalent displacements, we employ strains, which, in turn, requires one to specify a local characteristic length. Finally, the presence of in-plane shear stress brings about further modifications to the model as discussed below.

The equivalent displacement and stress for the four different damage modes are given as follows:

- Longitudinal tension:

$$\hat{\delta}_{1+} = \langle \delta_{11} \rangle, \quad (42)$$

$$\hat{S}_{1+} = \frac{\langle \hat{S}_{11} \rangle \langle \delta_{11} \rangle}{\hat{\delta}_{1+}}. \quad (43)$$

- Longitudinal compression:

$$\hat{\delta}_{1-} = \langle -\delta_{11} \rangle, \quad (44)$$

$$\hat{S}_{1-} = \frac{\langle -\hat{S}_{11} \rangle \langle -\delta_{11} \rangle}{\hat{\delta}_{1-}}. \quad (45)$$

- Transverse tension:

$$\hat{\delta}_{2+} = \sqrt{\langle \delta_{22} \rangle^2 + \delta_{12}^2}, \quad (46)$$

$$\hat{S}_{2+} = \frac{\langle \hat{S}_{22} \rangle \langle \delta_{22} \rangle + \hat{S}_{12} \delta_{12}}{\hat{\delta}_{2+}}. \quad (47)$$

- Transverse compression:

$$\hat{\delta}_{2-} = \sqrt{\langle -\delta_{22} \rangle^2 + \delta_{12}^2}, \quad (48)$$

$$\hat{S}_{2-} = \frac{\langle -\hat{S}_{22} \rangle \langle -\delta_{22} \rangle + \hat{S}_{12} \delta_{12}}{\hat{\delta}_{2-}}. \quad (49)$$

Here, $\delta_{\alpha\beta} = L_c \tilde{E}_{\alpha\beta}$, L_c is the characteristic length, and $\langle \cdot \rangle$ is the Macaulay bracket operator defined as

$$\langle x \rangle = \begin{cases} x & x \geq 0 \\ 0 & x < 0. \end{cases} \tag{50}$$

In order to take into account the presence of in-plane shear, the initial equivalent displacement and the material strength are re-expressed as follows (see [26]):

$$\hat{\delta}_i^0 = \hat{\delta}_i / \sqrt{F_i}, \tag{51}$$

$$\hat{S}_i^0 = \hat{S}_i / \sqrt{F_i}, \tag{52}$$

where $i = (1+, 1-, 2+, 2-)$ and F_i 's are defined in Eqs. (23)–(26). Note that in the case of uniaxial loading $\hat{\delta}_i^0$ and \hat{S}_i^0 reduce to the constant values assumed in a 1D progressive damage model. In the presence of shear $\hat{\delta}_i^0$ and \hat{S}_i^0 are no longer constant and depend on the solution.

Remark. From the bilinear model, the relationship between the characteristic length L_c , fracture energy G , and damage displacement ratio r is

$$G = \frac{r L_c (\hat{S}^0)^2}{2 E_Y^0}, \tag{53}$$

where E_Y^0 is the Young modulus. As a result, the three parameters are not independent and need to be set in a consistent manner. Furthermore, if L_c is assumed to be the same for all damage modes, it is evident from inspection of (42)–(49) and (41) that L_c cancels out and the results are not affected by it. In this case, the damage displacement ratio is the only one of the above three parameters that needs to be set.

Remark. The irreversibility of damage evolution may be expressed by means of the so-called Karush–Kuhn–Tucker (KKT) conditions (see, e.g., [16] for the use of KKT conditions in damage modeling). We introduce the damage loading function

$$f = \hat{\delta}(\tilde{E}) - \hat{\delta}, \tag{54}$$

where $\hat{\delta}(\tilde{E})$ is the equivalent displacement computed from the strain, and $\hat{\delta}$ is the history variable that starts at a threshold value and records the largest value attained by $\hat{\delta}(\tilde{E})$ beyond the threshold. Clearly, by its definition, $f \leq 0$, since $f = 0$ during the progressive damage evolution and $f < 0$ otherwise. Next we consider the relationship between the damage variable d and the equivalent displacement $\hat{\delta}$ given by Eq. (40), and take its rate of change to obtain

$$\dot{d} = \frac{\hat{\delta}^0 \hat{\delta}^f (\hat{\delta}^f - \hat{\delta})}{\hat{\delta}^2 (\hat{\delta}^f - \hat{\delta}^0)^2} \dot{\hat{\delta}}. \tag{55}$$

Since in the above equation $\frac{\hat{\delta}^0 \hat{\delta}^f (\hat{\delta}^f - \hat{\delta})}{\hat{\delta}^2 (\hat{\delta}^f - \hat{\delta}^0)^2} > 0$ for $\hat{\delta} \in (\hat{\delta}^0, \hat{\delta}^f)$, the condition $\dot{d} \geq 0$ is satisfied if $\dot{\hat{\delta}} \geq 0$. In summary, we find that the conditions $f \leq 0$, $\dot{\hat{\delta}} \geq 0$, and $f \dot{\hat{\delta}} = 0$, known as the KKT conditions, express the irreversibility of damage evolution. The latter equation follows from the fact that when progressive damage evolves (i.e., $\dot{\hat{\delta}} > 0$), the history variable is constantly updated, which gives $f = 0$.

3.5. Implementation of the constitutive model

The following procedure gives an implementation of the above described constitutive damage model. At each quadrature point on the shell midsurface we cycle over the lamina that comprise a composite laminate at this location. For each lamina we perform the following sequence of operations:

- Compute the Green–Lagrange strain $\tilde{\mathbf{E}}$ in the lamina coordinate system. Note that the strain has both membrane and bending contributions as in Eq. (4).

Table 1
Summary of the laminate type, materials employed, and loading conditions.

Laminate	Material	Loading case
[0/±45/90] _s	AS4/3501-6	7. Uniaxial loading: $h_y/h_x = 1/0$ 8. Biaxial loading: $h_y/h_x = 2/1$

- Compute the second Piola–Kirchhoff stress as $\tilde{\mathbf{S}} = \tilde{\mathbf{C}}\tilde{\mathbf{E}}$, where the constitutive tensor $\tilde{\mathbf{C}}$ reflects the current damaged state, and is obtained from Eq. (34). (Note that each lamina in a composite laminate has its own set of damage variables and indices.)
- Compute the effective second Piola–Kirchhoff stress $\hat{\mathbf{S}} = \mathbf{M}\tilde{\mathbf{S}}$, where the damage operator \mathbf{M} reflects the current damaged state and is given by Eq. (28).
- Using the effective second Piola–Kirchhoff stress evaluate the damage initiation functions F_i , $i = (1+, 1-, 2+, 2-)$ from Eqs. (23)–(26).
- For each damage mode compute the equivalent displacement $\hat{\delta}_i$ and stress \hat{S}_i using Eqs. (42)–(49), and their initial counterparts $\hat{\delta}_i^0$ and \hat{S}_i^0 using Eqs. (51)–(52).
- Compute the final equivalent displacement at full damage as $\hat{\delta}_i^f = 2G_i/\hat{S}_i^0$ or, alternatively, as $\hat{\delta}_i^f = r_i\hat{\delta}_i^0$, where r_i and G_i are the damage displacement ratio and fracture energy, respectively, for each mode i . (In the case when G_i is not known for a given damage mode, we need to make an assumption about the damage displacement ratio.)
- Update the damage variables d_i using Eq. (41), and use them to compute new damage indices d_1 – d_6 from Eqs. (35)–(37).
- Update the constitutive tensor $\tilde{\mathbf{C}}$ using Eq. (34) evaluated using the updated damage indices.

Once the updated constitutive tensors are computed for each lamina, we perform through-thickness homogenization using Eqs. (17)–(21), which yields the updated extensional (**A**), coupling (**B**), and bending (**D**) stiffnesses. The remaining parts of the Kirchhoff–Love shell formulation are as reported previously (see, e.g., [18,19]).

4. Numerical results

In this section we present several numerical examples that make use of the above described damage model. All the computations are performed using a NURBS-based discretization. Although the bending-strip terms are present in Eq. (16), bending strips are not used in any of the examples presented, either due to simple single-patch geometry or in-plane loading employed.

4.1. Laminated plate subjected to uniaxial and biaxial tensile loading

In 1998, a so-called *World-Wide Failure Exercise (WWFE)* was launched by the organizers Hinton and Soden [45–47] with the goal to assess the predictive power of the current approaches for modeling failure in composite laminates. The organizers chose a series of test cases embodying a wide range of input parameters for laminates, performed the experiments, and provided basic material data to the participants. The participants were invited to use their own theories and computational tools to blindly predict the results of the test cases without prior access to the experimental data. In the end, the experimental results were published together with the predictions reported by the participants. The failure theories and models employed by the participants are summarized in [47]. To the best of the author’s knowledge, this is the first time the damage model presented is validated using the WWFE test cases.

Here we test the damage model using two cases from [46]: Carbon fiber reinforced composite laminate (AS4/3501-6) with layup [0/±45/90]_s¹ under uniaxial (Case 7) and biaxial (Case 8) tensile loading [46], as summarized in Table 1. The laminate total thickness is 1.1 mm, and all the plies have the same thickness. Material properties of the lamina are given in Table 2.

The computations are performed on a square domain of size 5.0 × 5.0 mm using a NURBS mesh of 9 × 5C¹-continuous quadratic elements. The tensile load is applied as a traction boundary condition, and the loading level is gradually increased until the failure stress is reached.

¹ Subscript ‘s’ indicates symmetric layup.

Table 2
Material properties of AS4/3501-6 lamina.

Longitudinal modulus E_1 (GPa)	126
Transverse modulus E_2 (GPa)	11
In-plane shear modulus G_{12} (GPa)	6.6
Major Poisson's ratio ν_{12}	0.28
Longitudinal tensile strength X_T (MPa)	1950
Longitudinal compressive strength X_C (MPa)	1480
Transverse tensile strength Y_T (MPa)	48
Transverse compressive strength Y_C (MPa)	200
In-plane shear strength Z_L (MPa)	79
Characteristic length L_c (mm)	0.5

Table 3
Comparison of failure stress under uniaxial loading.

Failure stage	Failure mode/location	Failure stress (MPa)		
		IGA	Experiment	WWFE
Initial	Matrix/0° and ±45° plies	214	400	15–241
Final	Fiber/90° plies	660	718	385–728

Table 4
Comparison of failure stress under biaxial loading.

Failure stage	Failure mode/location	Failure stress (MPa)		
		IGA	Experiment	WWFE
Initial	Matrix/0° and ±45° plies	240	450	15–256
Intermediate	Matrix/90° plies	460	N/A	N/A
Final	Fiber/90° plies	790	808	320–840

Remark. Given the simple loading conditions, and the resulting constant strain state in the specimen, the computation could have been performed using a single linear element without changing the outcomes. It is really the damage model and not the discretization that is tested in this example.

The stress–strain curves for both loading cases are plotted in Fig. 5, and are compared with the experimental data from [48]. Because fracture energy is not specified for this case, we employ three different damage displacement ratios, $r = 1.05, 1.80,$ and 2.50 , and examine the effect of this parameter on the computed results. In general, there is good agreement between the experimental data and numerical results, although some deviation is observed, especially for the uniaxial loading case. Even with different damage displacement ratios the three curves generally overlap, except in regions where damage occurs. The damage displacement ratio that is close to unity causes an abrupt slip of the strain, and the material quickly transitions to the damaged state. Transition to the damaged state is much smoother for larger damage displacement ratios.

Tables 3 and 4 report the numerically predicted and experimentally measured failure stress (and failure modes) for the two loading cases considered. The initial and, in the case of biaxial loading, the intermediate failure stress are also reported in the Tables. Note that the predicted failure stress is insensitive to the damage displacement ratio parameter, which is an important finding of this study. The ranges of the failure stress predicted by the WWFE participants are also reported in the table. The variation in the data is considerable, suggesting further improvements in composite damage modeling are desired. Compared with other methods, the present model is among the best in predicting failure strength of composite laminates.

4.2. Notched composite laminate under uniaxial stress

Failure mechanisms in notched composites (i.e., composites with geometrical features present) were extensively investigated over the last several decades. In the notched case failure is driven by stress concentration around geometric

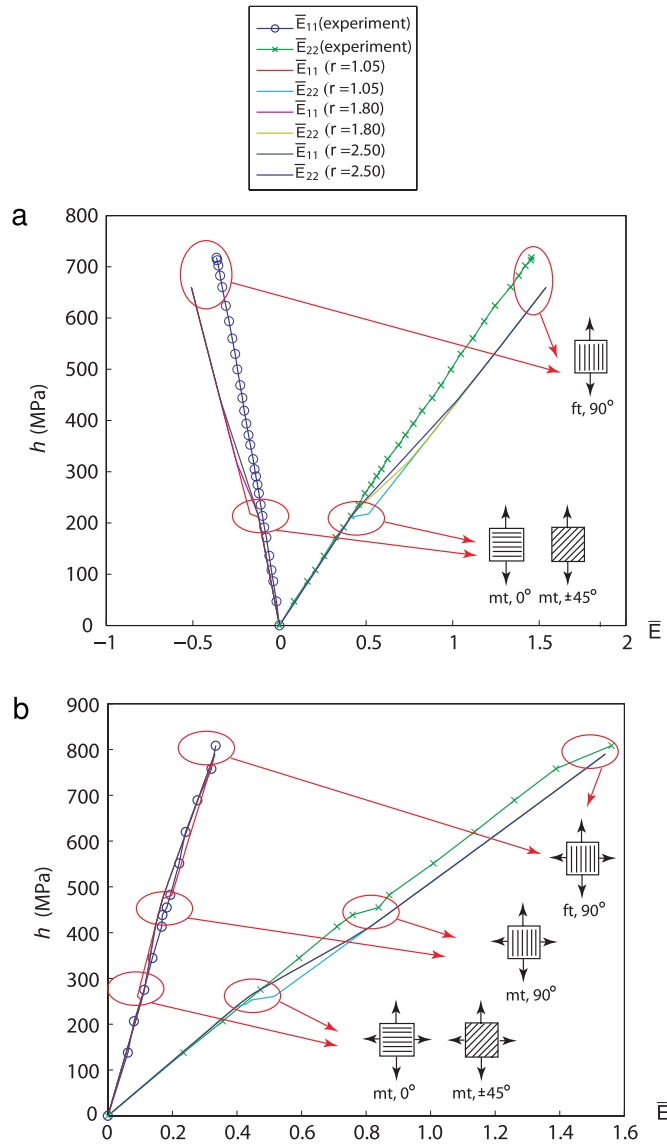


Fig. 5. Stress–strain curves for the two loading cases: (a) Uniaxial tension $h_y/h_x = 1/0$; (b) Biaxial tension $h_y/h_x = 2/1$.

features, and exhibits a wide range of effects. The notched strength depends on many factors, including laminate size and thickness, ply orientation, stacking sequence, and notch size. Investigations of the notch size effect show that even for configurations with the same stress concentration factor there may be large differences in both failure stress and failure mechanisms present [49,50].

There are three distinct types of failure mechanisms: pull-out, brittle, and delamination. The pull-out failure mechanism is dominated by fiber breaking with a lot of delamination and matrix cracking. The brittle failure mechanism is dominated by fiber failure with little or no delamination. In references [49,50], two scaled series of quasi-isotropic $[45/90/-45/0]_s$ carbon/epoxy (IM7/8852) specimens were tested and compared: a sub-laminate-level scaling, where the basic sub-laminate is repeated as $[45/90/-45/0]_{ns}^2$; and a ply-level scaling, where plies of the same orientation are stacked together as $[45_n/90_n/-45_n/0_n]_s$ to increase the effective ply thickness.

² Subscript 'n' indicates the number of times a stacking sequence is repeated in the laminate.

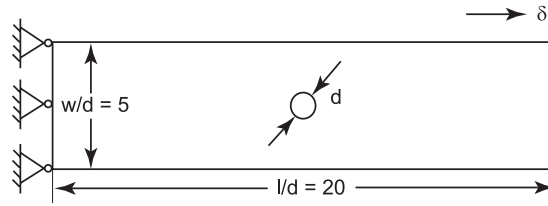


Fig. 6. Notched composite laminate geometry.

Table 5
Geometric parameters of notched composite laminate.

Laminate thickness t (mm)	Specimen width w (mm)	Gauge length l (mm)	Hole diameter d (mm)
4	63.5	254	12.7

Table 6
Material properties of the IM7/8552 lamina [51].

Longitudinal modulus, E_1 (GPa)	161
Transverse modulus, E_2 (GPa)	11.38
In-plane shear modulus, G_{12} (GPa)	5.17
Major Poisson's ratio, ν_{12}	0.32
Longitudinal tensile strength, X_T (MPa)	2608
Longitudinal compressive strength, X_C (MPa)	1731
Transverse tensile strength, Y_T (MPa)	76
Transverse compressive strength, Y_C (MPa)	275
In-plane shear strength, Z_L (MPa)	90
Fiber tensile damage displacement ratio, r_{ft}	4.0
Fiber compressive damage displacement ratio, r_{fc}	4.0
Matrix tensile damage displacement ratio, r_{mt}	2.0
Matrix compressive damage displacement ratio, r_{mc}	2.0

Here we simulate failure of a sub-laminate-level-scaled composite with stacking sequence $[45/90/-45/0]_{4s}$, and with thickness of 0.125 mm per lamina. This is one of the cases reported in [49] where the specimen failed in a brittle manner with little evidence of delamination, a failure type for which our model is valid. The geometric and material properties of the specimen are summarized in Fig. 6 and Tables 5 and 6. The left edge of the specimen is fixed, and the displacement δ is applied at the right edge, as shown in Fig. 6. We start by performing quasi-static analysis with displacement control, and continue up to nearly $\delta = 1.55$ mm. We then switch to a fully dynamic analysis in order to capture an abrupt drop in the load as the composite laminate fails. The dynamic portion of the analysis is performed using the Generalized- α method [52], where the right edge of the specimen is moved using a very slow displacement rate of 0.06 mm/min in order to avoid introducing the inertial effects.

Four quadratic NURBS meshes of 112, 448, 1792 and 7168 elements are employed in the computations. Meshes, shown in Fig. 7, are generated using global h -refinement. The specimen geometry is represented exactly in all cases due to the quadratic NURBS discretization employed.

In Fig. 8(a) the stress–displacement curves are plotted for the IGA simulations together with the experimental results from [49]. Convergence of the predicted failure stress under mesh refinement is shown in Fig. 8(b). The predicted laminate failure stress for the coarse, medium, fine, and finer mesh is 398.3 MPa, 375.6 MPa, 388.0 MPa, 387.6 MPa respectively, with the corresponding failure displacement of 1.675 mm, 1.575 mm, 1.628 mm and 1.626 mm, respectively. The experimental value for the laminate failure stress is 374 MPa. (The failure displacement is not reported in the experiments.) The IGA results compare well with the experimental data, and also exhibit good convergence under mesh refinement.

Fig. 9 shows the evolution of transverse second Piola–Kirchhoff stress \tilde{S}_{22} and the corresponding damage index d_2 in a 45° ply. Fig. 10 shows the evolution of the transverse second Piola–Kirchhoff stress S_{22} and the corresponding

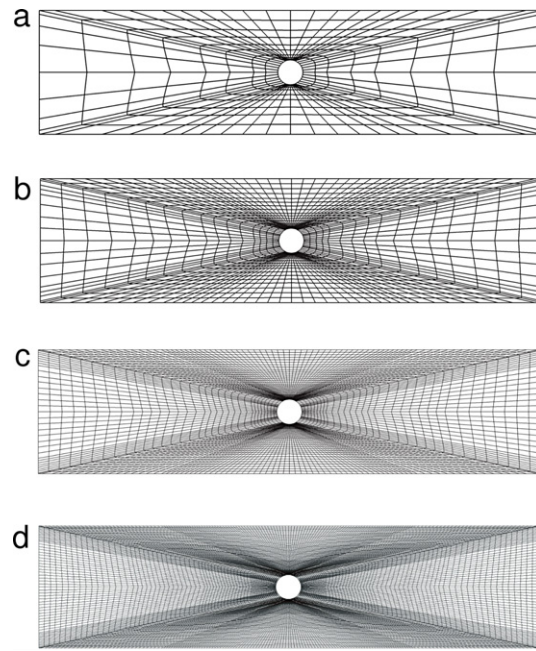


Fig. 7. Meshes of notched composite laminate: (a) Coarse; (b) Medium; (c) Fine; (d) Finer.

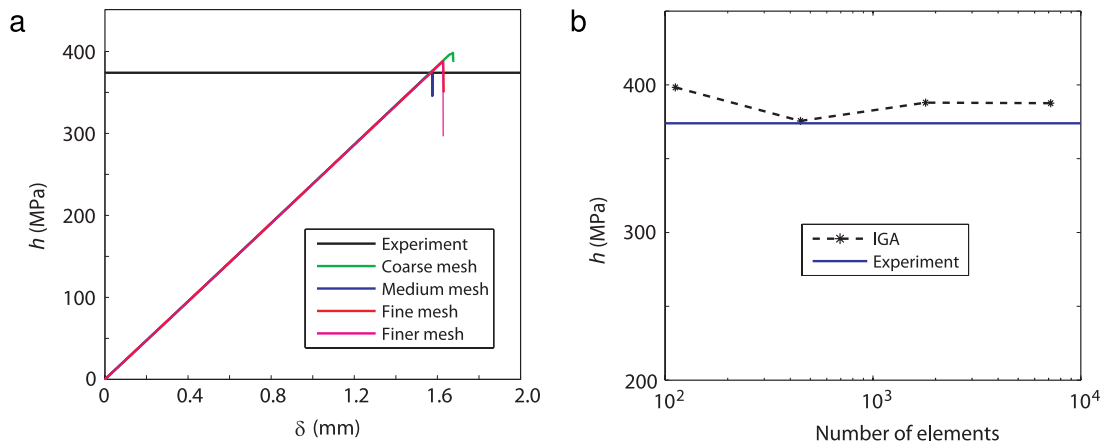


Fig. 8. (a) Stress–displacement curves for notched composite laminate; (b) Convergence of the failure stress. Results for all meshes are plotted and compared to failure-stress experimental data.

damage index d_2 in a 90° ply. In the figures we zoom on the region near a circular notch where the solution is most interesting. A non-symmetric stress solution is observed in a 45° ply, which precludes the use of quarter-symmetry in the simulations. The figures show how the developing material damage causes the redistribution of the internal stress and eventually leads to the specimen complete failure. Damage initiates at the top and bottom locations of the circular hole, which are the areas of largest stress concentrations for the loading considered. Regions of high stress then travel around the edges of the hole as well as toward the top and bottom edges of the specimen. The damage field follows the regions of high stress. Eventually, the entire vertical cross-section is damaged, and the laminate fails.

Fig. 11 shows the transverse second Piola–Kirchhoff stress \tilde{S}_{22} and the corresponding damage index d_2 in a 45° ply at failure for the medium, fine, and finer mesh resolution. Here we zoom even closer to the notch. Both the stress and damage profile show consistent convergence toward a smooth spatial distribution. Although no additional regularization (e.g., gradient-enhanced damage) is employed, localization of deformation is not observed in the results suggesting that some implicit regularization is likely present in our formulation. This regularization may be

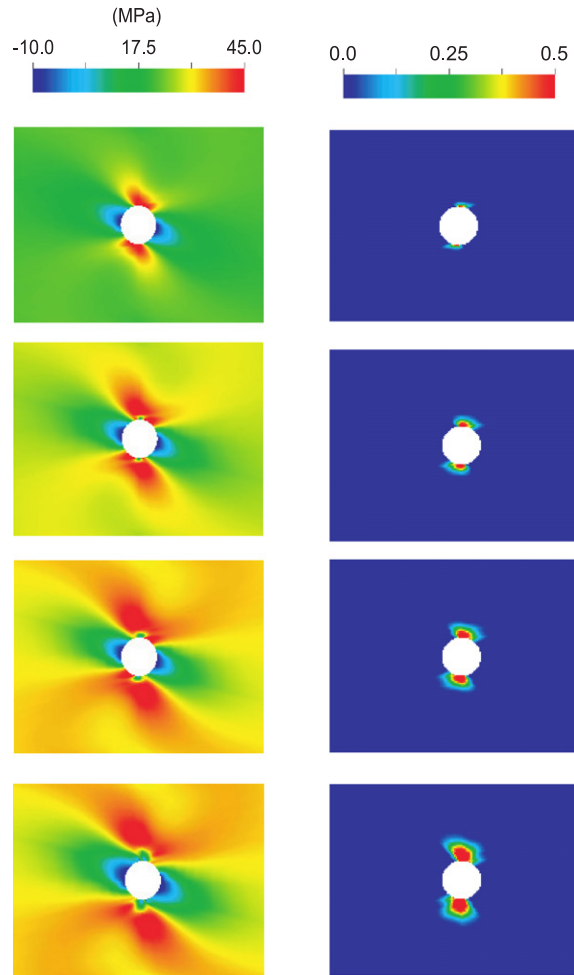


Fig. 9. Transverse stress \bar{S}_{22} (left) and transverse damage index d_2 (right) in a 45° ply. Top-to-bottom: $\delta = 1.08$ mm, $\delta = 1.395$ mm, $\delta = 1.575$ mm, and δ slightly larger than 1.575 mm, at failure.

attributable to: 1. The use of smooth NURBS functions, which implicitly regularize the strain and stress fields that, in turn, drive the damage variable evolution; 2. The use of through-thickness homogenization over multiple composite layers given by Eqs. (17)–(22).

4.3. Multiscale analysis of a plate under out-of-plane displacement loading

In this simple example involving a composite plate we show an application of a multiscale paradigm to composite damage modeling using Kirchhoff–Love shell analysis. The plate is made of carbon–epoxy composite and its schematic is shown in Fig. 12. The stacking sequence is $[0^\circ/90^\circ/0^\circ]$, and the plate total thickness is 8 mm.

To obtain the basic material properties of the undamaged specimen (i.e., the elastic moduli and Poisson’s ratio) we first develop a micromechanical computational model. A representative volume element (RVE) corresponding to a unit cell modeling a given fiber packing configuration is used to obtain homogenized material properties of a unidirectional carbon–epoxy fiber–reinforced composite [53]. The components of the homogenized elastic stiffness constitutive tensor are calculated by solving, in 3D, six independent micromechanical boundary value problems (BVPs) posed on the RVE. Each BVP corresponds to a linearly-elastic problem subject to the application of a macrostrain and periodic boundary conditions (see, e.g., [5–7]). The geometric and material properties of the RVE are provided in Tables 7 and 8, respectively. The schematic of the RVE and von Mises stress distribution due to axial loading transverse to the fiber direction are shown in Fig. 13. Table 9 provides the computed homogenized material properties of the carbon–epoxy

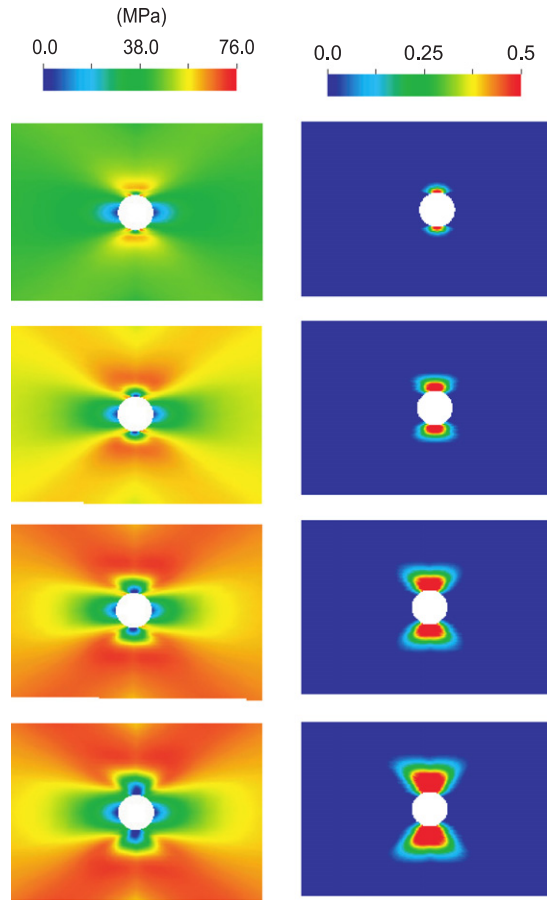


Fig. 10. Transverse stress \tilde{S}_{22} (left) and transverse damage index d_2 (right) in a 90° ply. Top-to-bottom: $\delta = 1.08$ mm, $\delta = 1.395$ mm, $\delta = 1.575$ mm, and δ slightly larger than 1.575 mm, at failure.

Table 7
RVE geometric parameters.

Fiber volume fraction	0.2
Fiber diameter d (μm)	3.5
RVE side length a (μm)	7.0

Table 8
RVE material properties.

	Young's modulus E (GPa)	Poisson's ratio ν
Carbon fiber	210	0.3
Epoxy matrix	4.6	0.4

fiber-reinforced composite. Theoretical estimates for the material properties of the composite are also provided for comparison, and good agreement is achieved between the computed and theoretical results. Note that the theoretical values for E_1 and ν_{12} are calculated by rules of mixtures, while the theoretical values for E_2 and G_{12} are calculated by the Halpin–Tsai relations [54].

The computed homogenized material properties of the composite lamina are employed in the composite-plate damage computations. The remaining material parameters related to the damage model are provided in Table 10. The

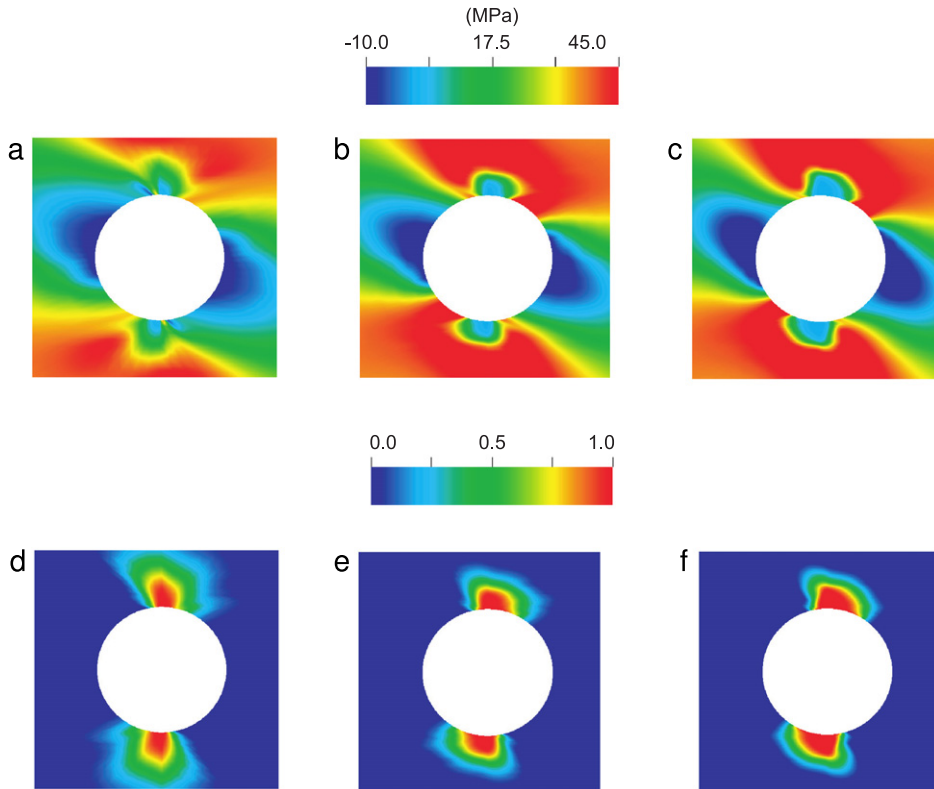


Fig. 11. Transverse stress \tilde{S}_{22} (top) and transverse damage index d_2 (bottom) in a 45° ply at failure. Left-to-right: Medium, fine, and finer mesh solution. Note the consistent convergence of the stress and damage index to a smooth spatial distribution.

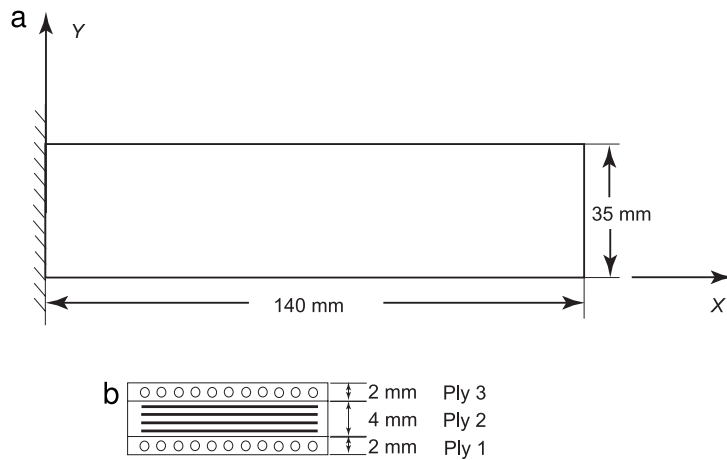


Fig. 12. Composite plate under out-of-plane displacement loading (in the $-z$ direction): (a) Plane view; (b) Cross-section view.

mesh of $9 \times 5C^1$ -continuous quadratic NURBS is employed in the computation. The plate is cantilevered on the left edge and is driven by a prescribed out-of-plane vertical displacement on the right edge. The total applied displacement is $\delta = 50$ mm and the plate is loaded quasi-statically until the final right-edge displacement is achieved.

Distribution of the transverse second Piola–Kirchhoff stress \tilde{S}_{22} and damage variable d_2 in the 90° ply are presented in Fig. 14. Prior to damage initiation, as shown in Fig. 14, maximum stress occurs at the left (i.e., fixed) edge of the plate. The damage first appears in that location, and, as the applied right-edge displacement is increased, the high-stress and damage fronts propagate toward the right side of the plate.

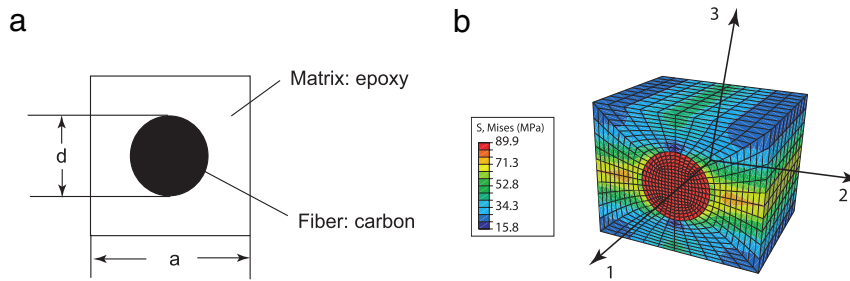


Fig. 13. (a) RVE cross-section; (b) Distribution of von Mises stress due to axial loading transverse to the fiber direction. Axial strain $\bar{\epsilon}_{22} = 0.01$ is applied to the RVE.

Table 9
Homogenized RVE material properties.

	Theoretical results	Numerical results
Longitudinal normal modulus E_1 (GPa)	45.68	44.33
Transverse normal modulus E_2 (GPa)	8.15	7.74
Longitudinal shear modulus G_{12} (GPa)	2.424	2.405
Longitudinal Poisson's ratio ν_{12}	0.38	0.378

Table 10
Material properties of the carbon–epoxy composite.

Longitudinal tensile strength X_T (MPa)	1500
Longitudinal compressive strength X_C (MPa)	1200
Transverse tensile strength Y_T (MPa)	45
Transverse compressive strength Y_C (MPa)	250
In-plane shear strength Z_L (MPa)	60
Fiber tensile fracture energy G_{ft} (kJ m ⁻²)	20
Fiber compressive fracture energy G_{fc} (kJ m ⁻²)	20
Matrix tensile fracture energy G_{mt} (kJ m ⁻²)	2.5
Matrix compressive fracture energy G_{mc} (kJ m ⁻²)	2.5
Characteristic length L (mm)	0.5

The force–displacement curve for the composite plate is plotted in Fig. 15. Standard FEM results obtained using commercial software ABAQUS/Standard 6.10 [55], computed using a four-node shell element based on the Reissner–Mindlin theory, with reduced integration and a similar damage model, are plotted for comparison. Both curves generally produce good agreement. Minor deviation between the curves is observed at higher levels of deformation, which is likely due to the fact that the through-thickness transverse shear is ignored in the Kirchhoff–Love shell theory.

Remark. In this example the purpose of including a simple RVE model is to establish the framework for the multiscale analysis of composite damage in isogeometric shells alluded to in the introduction. The RVE model may be further enhanced with, for example: Cohesive elements/zones [56] to simulate the debonding of the fiber–matrix interface; XFEM [57] or phase-field [58] formulation to simulate the growth and coalescence of microcracks; Multiple adaptive levels [6,7] to simulate random distribution of fibers. With such enhancements, a more complete (and realistic) set of damage model parameters may be obtained.

Remark. Both the IGA and FEM computations assume that for this case no delamination will occur, as only intralaminar damage modes are considered in the models. This assumption is valid for this example if the interlaminar strength of the specimen is high enough. In the case of low interlaminar strength, a full analysis with delamination would be necessary to obtain physically realistic results.

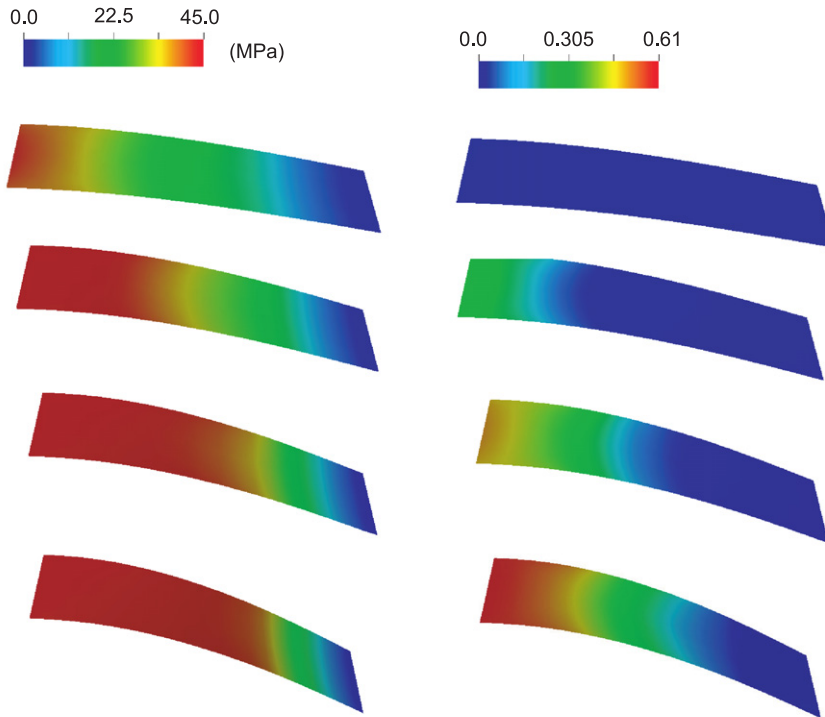


Fig. 14. Transverse stress \tilde{S}_{22} (left) and transverse damage index d_2 (right) in a 90° top ply. Top-to-bottom: $\delta = 19.5$ mm, $\delta = 30$ mm, $\delta = 40$ mm, and $\delta = 50$ mm.

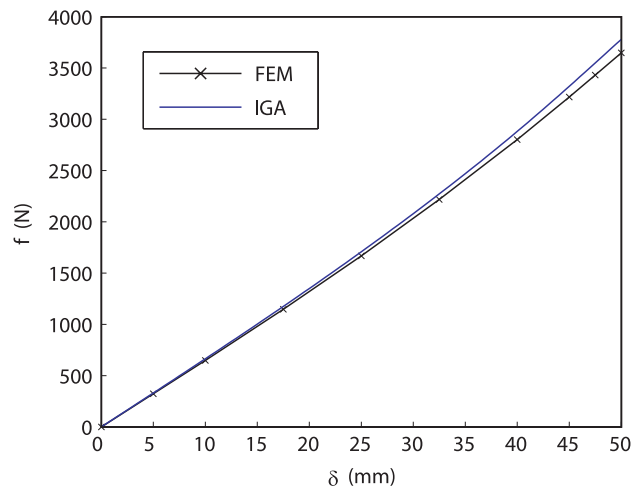


Fig. 15. Force–displacement curve for the composite plate. Comparison of the IGA and FEM results.

5. Conclusions and future work

In this paper a recently proposed large-deformation isogeometric Kirchhoff–Love shell formulation is enhanced with a damage model, which enables the simulation of progressive damage in laminated composite structures. The damage model consists of Hashin’s theory for damage initiation, and a bilinear material model for damage evolution. Four intralaminar modes of failure – longitudinal and transverse tension, and longitudinal and transverse compression – are considered. The model is valid in the regime of relatively thin shell structures where through-thickness transverse shear may be ignored and where damage occurs without significant evidence of delamination.

Special attention is paid to model validation and behavior under mesh refinement. The computation of damage in an unnotched carbon-fiber–reinforced laminate (AS4/3501-6) revealed that the present model is among the best in predicting failure strength of composite laminates. However, the results of the present study as well as those reported by the participants of the ‘World-Wide Failure Exercise’ (WWFE) indicate that the initial failure stress is significantly underpredicted by all the models, while some of the models, including the present one, are able to predict the final failure stress quite well. The large spread in the data reported by the WWFE participants indicates the lack of consensus regarding failure modeling in laminated composites, and suggests that further research is necessary to improve the predictive power of failure models.

The computation of damage in a carbon-fiber–reinforced laminate (IM7/8552) with a circular notch showed very good agreement with the experimental data. Good convergence of the failure stress and displacement under mesh refinement were also observed. This good accuracy of the simulations and a consistent convergence pattern is attributable to the exact specimen geometry representation, and to the use of an IGA discretization of higher order and continuity. Besides exhibiting good numerical properties the model produced valuable data on how the stress redistributes in the complex-geometry specimen as the damage inside it initiates and evolves.

In this paper the damage model is also illustrated in the context of multiscale composite damage analysis. An appropriate micromechanical model based on an RVE representing a given fiber packing configuration is used to compute the lamina material properties employed in a macroscale computation of a composite plate damage. The ability to use the model in the context of multiscale composite damage analysis opens way for its use in full-scale composite structures, such as modern aircraft fuselage and wings, and wind-turbine blades. Although the main objectives of this paper were to develop and present an IGA-based composite damage modeling framework, and to perform its careful validation using actual experimental data at the coupon level, current efforts are underway to integrate the framework with realistic large-scale structural designs. In particular, of great interest is the integration of the current framework with Dynamic Data-Driven Application Systems (DDDAS) [59] for large-scale composite structures.

Other future directions for IGA-based damage modeling in composites is to incorporate more complex through-thickness behavior to enable modeling of delamination, which to this day presents a significant challenge. One pathway to delamination modeling is the recently proposed continuum or solid-like shell formulations [60,61]. High-cycle fatigue damage presents another important research direction. Finally, although strain localization and the associated mesh sensitivity was not observed in the examples computed in this paper, such phenomena may occur even in the context of smooth IGA discretizations, and would require appropriate modeling and numerical treatment, such as, for example, using a nonlocal, gradient-enhanced damage model [8–11].

Acknowledgments

The corresponding author and the second author were supported through AFOSR Award FA9550-12-1-0005. The first author was supported through AFOSR Award FA9550-12-1-0046. This support is gratefully acknowledged. The authors would also like to express their gratitude to Prof. Hyonny Kim, Structural Engineering, UC, San Diego, for fruitful discussions about failure in composite laminates and for pointing us to the World-Wide Failure Exercise references.

References

- [1] J. Fish, Q. Yu, Two-scale damage modeling of brittle composites, *Compos. Sci. Technol.* 61 (2001) 2215–2222.
- [2] S. Kruch, J.L. Chaboche, T. Pottier, Two-scale viscoplastic and damage analysis of metal matrix composite, *Stud. Appl. Mech.* 44 (1996) 45–56.
- [3] J. Fish, Q. Yu, Computational damage mechanics for composite materials based on mathematical homogenization, *Internat. J. Numer. Methods Engrg.* 45 (1999) 1657–1679.
- [4] M.V.C. Alfaro, A.S.J. Suiker, C.V. Verhoosel, R. de Borst, Numerical homogenization of cracking processes in thin fibre-epoxy layers, *Eur. J. Mech. A Solids* 29 (2010) 119–131.
- [5] P. Raghavan, S. Li, S. Ghosh, Two scale response and damage modeling of composite materials, *Finite Elem. Anal. Des.* 40 (2004) 1619–1640.
- [6] S. Swaminathan, S. Ghosh, N.J. Pagano, Statistically equivalent representative volume elements for composite microstructures, part i: Without damage, *J. Compos. Mater.* 40 (2006) 583–604.
- [7] S. Swaminathan, S. Ghosh, Statistically equivalent representative volume elements for composite microstructures, part ii: With evolving damage, *J. Compos. Mater.* 40 (2006) 605–621.

- [8] G. Pijaudier-Cabot, Z.P. Bazant, Nonlocal damage theory, *J. Eng. Mech.* 113 (1987) 1512–1533.
- [9] Z.P. Bazant, G. Pijaudier-Cabot, Nonlocal continuum damage, localization instability and convergence, *J. Appl. Mech.* 55 (1988) 287–293.
- [10] R. de Borst, J. Pamin, R.H.J. Peerlings, L.J. Sluys, Strain-based transient-gradient damage model for failure analyses, *Comput. Mech.* 17 (1995) 130–141.
- [11] M.G.D. Geers, R. de Borst, W.A.M. Brekelmans, R.H.J. Peerlings, Strain-based transient-gradient damage model for failure analyses, *Comput. Methods Appl. Mech. Engrg.* 160 (1998) 133–153.
- [12] C.V. Verhoosel, M.A. Scott, T.J.R. Hughes, R. de Borst, An isogeometric analysis approach to gradient damage models, *Internat. J. Numer. Methods Engrg.* 86 (2011) 115–134.
- [13] T.J.R. Hughes, J.A. Cottrell, Y. Bazilevs, Isogeometric analysis: CAD, finite elements, NURBS, exact geometry, and mesh refinement, *Comput. Methods Appl. Mech. Engrg.* 194 (2005) 4135–4195.
- [14] J.A. Cottrell, T.J.R. Hughes, Y. Bazilevs, *Isogeometric Analysis: Toward Integration of CAD and FEA*, Wiley, Chichester, 2009.
- [15] L. Piegl, W. Tiller, *The NURBS Book (Monographs in Visual Communication)*, second ed., Springer-Verlag, New York, 1997.
- [16] S. Hosseini, J.J.C. Remmers, R. de Borst, The incorporation of gradient damage models in shell elements, *Comput. Methods Appl. Mech. Engrg.* 98 (2014) 391–398.
- [17] Y. Bazilevs, A.L. Marsden, F. Lanza di Scalea, A. Majumdar, M. Tatineni, Toward a computational steering framework for large-scale composite structures based on continually and dynamically injected sensor data, *Procedia Comput. Sci.* 9 (2012) 1149–1158.
- [18] J. Kiendl, K.-U. Bletzinger, J. Linhard, R. Wüchner, Isogeometric shell analysis with Kirchhoff–Love elements, *Comput. Methods Appl. Mech. Engrg.* 198 (2009) 3902–3914.
- [19] J. Kiendl, Y. Bazilevs, M.-C. Hsu, R. Wüchner, K.-U. Bletzinger, The bending strip method for isogeometric analysis of Kirchhoff–Love shell structures comprised of multiple patches, *Comput. Methods Appl. Mech. Engrg.* 199 (2010) 2403–2416.
- [20] D.J. Benson, Y. Bazilevs, M.-C. Hsu, T.J.R. Hughes, Isogeometric shell analysis: The Reissner–Mindlin shell, *Comput. Methods Appl. Mech. Engrg.* 199 (2010) 276–289.
- [21] D.J. Benson, Y. Bazilevs, M.-C. Hsu, T.J.R. Hughes, A large deformation, rotation-free, isogeometric shell, *Comput. Methods Appl. Mech. Engrg.* 200 (2011) 1367–1378.
- [22] D.J. Benson, S. Hartmann, Y. Bazilevs, M.-C. Hsu, T.J.R. Hughes, Blended isogeometric shells, *Comput. Methods Appl. Mech. Engrg.* 255 (2013) 133–146.
- [23] R. Echter, B. Oesterle, M. Bischoff, A hierarchic family of isogeometric shell finite elements, *Comput. Methods Appl. Mech. Engrg.* 254 (2013) 170–180.
- [24] Y. Bazilevs, M.-C. Hsu, J. Kiendl, R. Wüchner, K.-U. Bletzinger, 3D simulation of wind turbine rotors at full scale. Part II: Fluid–structure interaction modeling with composite blades, *Internat. J. Numer. Methods Fluids* 65 (2011) 236–253.
- [25] Y. Bazilevs, M.-C. Hsu, J. Kiendl, D.J. Benson, A computational procedure for prebending of wind turbine blades, *Internat. J. Numer. Methods Engrg.* 89 (2012) 323–336.
- [26] I. Lapczyk, J.A. Hurtado, Progressive damage modeling in fiber-reinforced materials, *Composites A* 38 (2007) 2333–2341.
- [27] Z. Hashin, A. Rotem, A fatigue criterion for fiber-reinforced materials, *J. Compos. Mater.* 7 (1973) 448–464.
- [28] A. Matzenmiller, J. Lubliner, R.L. Taylor, A constitutive model for anisotropic damage in fiber-composites, *Mech. Mater.* 20 (1995) 125–152.
- [29] C.A.M. Soares, C.M.M. Soares, M.J.M. Freitas, *Mechanics of Composite Materials and Structures*, Kluwer Academic Publishers, 1998.
- [30] M. Bischoff, W.A. Wall, K.-U. Bletzinger, E. Ramm, Models and finite elements for thin-walled structures, in: E. Stein, R. de Borst, T.J.R. Hughes (Eds.), *Encyclopedia of Computational Mechanics*, in: *Solids, Structures and Coupled Problems*, vol. 2, Wiley, 2004 (Chapter 3).
- [31] K.U. Bletzinger, M. Firl, J. Linhard, R. Wüchner, Optimal shapes of mechanically motivated surfaces, *Comput. Methods Appl. Mech. Engrg.* 199 (2010) 324–333.
- [32] K.U. Bletzinger, R. Wüchner, F. Daoud, N. Camprubí, Computational methods for form finding and optimization of shells and membranes, *Comput. Methods Appl. Mech. Engrg.* 194 (2005) 3438–3452.
- [33] E. Oñate, F. Zarate, Rotation-free triangular plate and shell elements, *Internat. J. Numer. Methods Engrg.* 47 (2000) 557–603.
- [34] F. Cirak, M. Ortiz, Fully C^1 -conforming subdivision elements for finite deformation thin-shell analysis, *Internat. J. Numer. Methods Engrg.* 51 (2001) 813–833.
- [35] J. Linhard, R. Wüchner, K.U. Bletzinger, “Upgrading” membranes to shells—the CEG rotation free shell element and its application in structural analysis, *Finite Elem. Anal. Des.* 44 (2007) 63–74.
- [36] T. Belytschko, W.K. Liu, B. Moran, *Nonlinear Finite Elements for Continua and Structures*, Wiley, 2000.
- [37] J.N. Reddy, *Mechanics of Laminated Composite Plates and Shells: Theory and Analysis*, second ed., CRC Press, Boca Raton, FL, 2004.
- [38] C.G. Davila, C.A. Rose, Lecture note: Progressive damage analysis of composites, in: *Aircraft Aging and Durability Project*, NASA, Brussels, Belgium, 2007.
- [39] I.M. Daniel, O. Ishai, *Engineering Mechanics of Composite Materials*, Oxford University Press, New York, NY, 1994.
- [40] S.T. Pinho, Modeling failure of laminated composites using physically-based failure models (Ph.D. thesis), Imperial College London, 2005.
- [41] P. Maimi, P.P. Camanho, J.A. Mayugo, C.G. Davila, A continuum damage model for composite laminates: Part i—constitutive model, *Mech. Mater.* 39 (2007) 897–908.
- [42] P. Maimi, P.P. Camanho, J.A. Mayugo, C.G. Davila, A continuum damage model for composite laminates: Part ii—computational implementation and validation, *Mech. Mater.* 39 (2007) 909–919.
- [43] A. Murakami, Mechanical modeling of material damage, *J. Appl. Mech. Trans. ASME* 55 (1988) 280–286.
- [44] S.H. Song, G.H. Paulino, W.G. Buttlar, Influence of the cohesive zone model shape parameter on asphalt concrete fracture behavior, *AIP Conf. Proc.* 973 (2008) 730–735.
- [45] M.J. Hinton, P.D. Soden, Predicting of failure in composite laminate: The background to the exercise, *Compos. Sci. Technol.* 58 (1998) 1001.

- [46] P.D. Soden, M.J. Hinton, A.S. Kaddour, Lamina properties, lay-up configurations and loading conditions for a range of fiber-reinforced composite laminates, *Compos. Sci. Technol.* 58 (1998) 1011–1022.
- [47] P.D. Soden, M.J. Hinton, A.S. Kaddour, A comparison of the predictive capabilities of current failure theories for composite laminates, *Compos. Sci. Technol.* 58 (1998) 1225–1254.
- [48] P.D. Soden, M.J. Hinton, A.S. Kaddour, Biaxial test result for strength and deformation of a range of e-glass and carbon fiber reinforced composite laminates: Failure exercise benchmark data, *Compos. Sci. Technol.* 62 (2002) 1489–1514.
- [49] B.G. Green, M.R. Wisnom, S.R. Hallett, An experimental investigation into tensile strength scaling of notched composites, *Composites* 38 (2007) 867–878.
- [50] S.R. Hallett, B.G. Green, W.G. Jiang, M.R. Wisnom, An experimental and numerical investigation into the damage mechanisms in notched composites, *Composites A* 40 (2009) 619–624.
- [51] M.J. Swindeman, E.V. Iarve, R.A. Brockman, D.H. Mollenhauer, S.R. Hallett, Strength prediction in open hole composite laminates by using discrete damage modeling, *AIAA J.* 51 (2013) 936–945.
- [52] J. Chung, G.M. Hulbert, A time integration algorithm for structural dynamics with improved numerical dissipation: The generalized- α method, *J. Appl. Mech.* 60 (1993) 371–375.
- [53] C.T. Sun, R.S. Vaidya, Prediction of composite properties from a representative volume element, *Compos. Sci. Technol.* 56 (1996) 171–179.
- [54] I.M. Daniel, O. Ishai, *Engineering Mechanics of Composite Materials*, Oxford University Press, 2006.
- [55] ABAQUS Inc. ABAQUS 6.10 User's manual. Providence, RI, USA, 2010.
- [56] C.V. Verhoosel, M.A. Scott, R. de Borst, T.J.R. Hughes, An isogeometric approach to cohesive zone modeling, *Internat. J. Numer. Methods Engrg.* 87 (2011) 336–360.
- [57] E. De Luycker, D.J. Benson, T. Belytschko, Y. Bazilevs, M.-C. Hsu, X-FEM in isogeometric analysis for linear fracture mechanics, *Internat. J. Numer. Methods Engrg.* 87 (2011) 541–565.
- [58] M.J. Borden, M.A. Scott, C.V. Verhoosel, T.J.R. Hughes, C.M. Landis, A phase-field description of dynamic brittle fracture, *Comput. Methods Appl. Mech. Engrg.* 217–220 (2012) 77–95.
- [59] F. Darema, Dynamic data driven applications systems: A new paradigm for application simulations and measurements, in: *Proceedings of ICCS 2004 4th International Conference on Computational Science, 2004*, pp. 662–669.
- [60] S. Hosseini, J.J.C. Remmers, C.V. Verhoosel, R. de Borst, An isogeometric solid-like shell element for non-linear analysis, *Internat. J. Numer. Methods Engrg.* 95 (2013) 238–256.
- [61] S. Hosseini, J.J.C. Remmers, C.V. Verhoosel, R. de Borst, An isogeometric continuum shell element for non-linear analysis, *Comput. Methods Appl. Mech. Engrg.* 271 (2014) 1–22.